Monthly Notices
of the
ROYAL ASTRONOMICAL SOCIETY

Mon. Not. R. Astron. Soc. **405,** 2327–2338 (2010) doi:10.1111/j.1365-2966.2010.16666.x

Composite star formation histories of early-type galaxies from minor mergers: prospects for WFC3

S. Peirani,[1,2⋆] R. M. Crockett,[2] S. Geen,[2] S. Khochfar,[3] S. Kaviraj[2,4] and J. Silk[2]

[1]*Institut d'Astrophysique de Paris, 98 bis Bd Arago, 75014 Paris, France – Unité mixte de recherche 7095 CNRS-Université Pierre et Marie Curie, Paris, France*
[2]*Department of Physics, University of Oxford, Denys Wilkinson Building, Keble Road, Oxford OX1 3RH*
[3]*Max Planck Institut für extraterrestrische Physik, PO Box 1312, D-85478 Garching, Germany*
[4]*Blackett Laboratory, Imperial College London, South Kensington Campus, London SW7 2AZ*

Accepted 2010 March 8. Received 2010 February 1; in original form 2009 December 11

ABSTRACT

The star formation history of nearby early-type galaxies is investigated via numerical modelling. Idealized hydrodynamical *N*-body simulations with a star formation prescription are used to study the minor merger process ($1/10 \leq M_1/M_2 \leq 1/4$; $M_1 \leq M_2$) between a giant galaxy (host) and a less massive spiral galaxy (satellite) with reasonable assumptions for the ages and metallicities of the merger progenitors. We find that the evolution of the star formation rate is extended over several dynamical times and shows peaks which correspond to pericentre passages of the satellite. The newly formed stars are mainly located in the central part of the satellite remnant while the older stars of the initial disc are deposited at larger radii in shell-like structures. After the final plunge of the satellite, star formation in the central part of the remnant can continue for several Gyr depending on the star formation efficiency. Although the mass fraction in new stars is small, we find that the half-mass radius differs from the half-light radius in the *V* and *H* bands. Moreover synthetic 2D images in *J*, *H*, NUV, Hβ and *V* bands, using the characteristic filters of the Wide Field Camera 3 (WFC3) on the *Hubble Space Telescope*, reveal that residual star formation induced by gas-rich minor mergers can be clearly observed during and after the final plunge, especially in the near-ultraviolet band, for interacting systems at ($z \leq 0.023$) over moderate numbers of orbits (approximately two orbits correspond to typical exposure times of $\sim$3600 s). This suggests that WFC3 has the potential to resolve these substructures, characterize plausible past merger episodes and give clues to the formation of early-type galaxies.

Key words: methods: miscellaneous – galaxies: formation – galaxies: interactions – galaxies: kinematics and dynamics – galaxies: photometry – galaxies: structure.

1 INTRODUCTION

The formation and evolution of early-type galaxies (ETGs) remain an outstanding puzzle in contemporary astrophysics (see Cimatti 2009 for a recent review). According to earlier studies, ETGs seem to form a class of objects with simple and well-defined properties: they tend to have a smooth morphology, an old stellar population, a red optical colour and are free of cold gas and ongoing star formation (Searle, Sargent & Bagnulo 1973; Larson 1975). However, this classic picture is challenged by recent observations. For instance, the presence of cold gas and dust as well as evidence of recent star formation has been detected in several systems (see, for instance, Goudfrooij et al. 1994; Macchetto et al. 1996; Trager et al. 2000; Yi et al. 2005; Morganti et al. 2006; Kaviraj et al. 2007; Sarzi et al. 2008, Clemens et al. 2009b), and the associated star formation rate (SFR) can even be comparable to that in normal spiral galaxies although these events are rather rare (Fukugita et al. 2007). Moreover, recent studies based on *Galaxy Evolution Explorer* (*GALEX*) near-UV photometry of a large sample of ETGs found that 30 per cent of them experience ongoing or recent star formation (Kaviraj et al. 2007; Schawinski et al. 2007), and a similar trend has been obtained from mid-infrared *Spitzer* data in the Coma and Virgo Clusters (Bressan et al. 2006; Clemens et al. 2009a) or from the COSMOS survey (Kaviraj et al. 2010).

Understanding the formation of ETGs, and in particular their star formation history, is of crucial importance for setting strong

⋆E-mail: peirani@iap.fr

constraints on models of galaxy formation. As has been widely discussed in the literature, there are currently two competing scenarios for the formation of ETGs. On the one hand, there is the *monolithic collapse* model in which galaxies are formed in short, highly efficient starbursts at high redshift ($z \gg 1$) and evolve purely passively thereafter (Eggen, Lynden-Bell & Sandage 1962; Larson 1974; Arimoto & Yoshii 1987). On the other hand, the *hierarchical structure formation* model suggests that the most massive galaxies are formed from successive mergers of smaller entities with accompanying star formation over a cosmological time-scale (Toomre 1977; Blumenthal et al. 1984; Kauffmann, White & Guiderdoni 1993). Although these models are in good agreement with some aspects of observational data, they both face some problems. For instance, the monolithic model is supported by the existence of, and small scatter in, galaxy scaling relations such as the colour–magnitude relation (Sandage & Visvanathan 1978), the Fundamental Plane (Djorgovski & Davis 1987; Jorgensen, Franx & Kjaergaard 1996; Saglia et al. 1997) and the Mg–σ relation (Colless et al. 1999; Kuntschner et al. 2001), but cannot easily explain the residual star formation and cold gas found in ETGs. As far as hierarchical models are concerned, although they predict galaxy interaction, they are in disagreement with the so-called downsizing phenomenon. Indeed, observations of deep surveys ($z \geq 1$–2), such as the Las Campanas Infrared Survey, *HST* Deep Field-North and Gemini Deep Deep Survey (GDDS), have revealed an excess of massive ETGs undergoing 'top-down' assembly with high inferred specific SFRs relative to predictions of the hierarchical scenario (Glazebrook et al. 2004; Kodama et al. 2004; Cimatti, Daddi & Renzini 2006).

It is now well known that ETGs have considerable substructure [e.g. from Spectrographic Areal Unit for Research on Optical Nebulae (SAURON) and *GALEX*] which is interpreted as a result of mergers in the past several Gyr. To study this plausible process, we have compared the ultraviolet (UV) colours of nearby ($0.05 \leq z \leq 0.06$) ETGs with synthetic photometry derived from numerical simulations of minor mergers, with reasonable assumption for the ages, metallicities and dust properties of the merger progenitors (Kaviraj et al. 2009, hereafter K09). We found that the large scatter in the UV colours of intermediate-mass ETGs in the local universe and the inferred low-level recent star formation in these objects can be reproduced by minor mergers in the standard Λ cold dark matter (ΛCDM) cosmology. In this work, our aim is to study the evolution of the internal structure of these objects using the same methodology but with higher mass resolution, in order to help understand in more detail the observational signatures of satellite minor merger events with different mass ratios, gas fractions and orbital configurations. This work is also motivated by the recent installation on the *Hubble Space Telescope* (*HST*) of NASA's Wide Field Camera 3 (WFC3[1]) whose optical design provides a large field of view (FOV) and high sensitivity over a broad wavelength range, excellent spatial resolution and a stable and accurate photometric performance. It features two independent imaging cameras, a UV/optical channel (UVIS) and a near-infrared channel (IR). Both channels are equipped with a broad selection of spectral filters, and some of these have been considered in our study in order to identify disrupted satellites and trace the history of the merger process.

This paper is organized as follows. In section 2, we summarize the numerical methodology that we have developed to produce WFC3 synthetic images; in Section 3, we present results on the star formation history of nearby ETGs, while Section 4 presents our conclusions.

[1]http://www.stsci.edu/hst/wfc3

2 NUMERICAL METHODOLOGY

2.1 Simulations

The numerical methodology used in this paper is described in detail in K09 where we refer the reader for more information. For the sake of clarity, we summarize the main steps below.

Our aim is to study minor mergers between an elliptical galaxy (E) and a satellite (spiral galaxy) using idealized N-body+smoothed particle hydrodynamics simulations. Both galaxies are created following Springel, Di Matteo & Hernquist (2005). First, the elliptical is modelled using a spherical dark matter (DM) halo and a stellar component, with a total mass of $10^{12}\,\mathrm{M}_{\odot}$. Stars contribute 4 per cent of this value in agreement with recent observational studies (see, for instance, Jiang & Kochanek 2007; McGaugh et al. 2010). A Hernquist profile reproduces the de Vaucouleurs $R^{1/4}$ surface brightness profiles of typical elliptical galaxies. The effective radius of the projected brightness is $r_{\mathrm{e}} = 4.29\,\mathrm{kpc}$. As far as the satellite is concerned, we used a compound galaxy model which consists of a spherical DM halo and a rotationally supported disc of gas and star (but no bulge) with independent parameters describing each of the structural components. The mass of the disc represents 5 per cent of the total mass of the satellite and the gas mass fraction in the disc is fixed to a constant value of 20 per cent (of the total mass of the disc), consistent with observed values from the Sloan Digital Sky Survey (SDSS; Kannappan 2004). In all simulations, satellites are put on prograde or retrograde parabolic orbits (Khochfar & Burkert 2006), with varying pericentric distances r_{p} and initial separations of $r_{\mathrm{ini}} = 100\,\mathrm{kpc}$.

The simulations are performed using the publicly available code GADGET2 (Springel 2005) with added prescriptions for cooling, star formation and feedback from Type Ia and II supernovae (SNe). It is worth mentioning that gas particles with $T < 2 \times 10^4\,\mathrm{K}$, number density $n > 0.1\,\mathrm{cm}^{-3}$, overdensity $\Delta\rho_{\mathrm{gas}} > 100$ and $\nabla\cdot\upsilon < 0$ form stars according to the standard star formation prescription: $\mathrm{d}\rho_*/\mathrm{d}t = c_*\rho_{\mathrm{gas}}/t_{\mathrm{dyn}}$, where ρ_* refers to the stellar density, t_{dyn} is the local dynamical time-scale of the gas and c_* is the star formation efficiency.

In this study, we use 10 times more particles than in K09 in order to more accurately study the evolution of the spatial distribution of stars. Consequently, ~4000 000 particles are used for each experiment in which the particle masses are $M_{\mathrm{DM}} = 3.03 \times 10^5\,\mathrm{M}_{\odot}$, $M_{\mathrm{gas}} = M_{\mathrm{disc}} = 4.5 \times 10^4\,\mathrm{M}_{\odot}$ and $M_{\mathrm{E}} = 1.35 \times 10^5\,\mathrm{M}_{\odot}$ for the DM particles, gas particles, star particles in the disc and star particles in the elliptical galaxy (E), respectively. The gravitational softening lengths (ϵ) used in each simulation are (*physical*) $\epsilon_{\mathrm{DM}} = \epsilon_{\mathrm{E}} = 0.1\,\mathrm{kpc}$ and $\epsilon_{\mathrm{gas}} = \epsilon_{\mathrm{disc}} = 0.2\,\mathrm{kpc}$. We have also checked that increasing the resolution of the simulations with respect to K09 does not affect the star formation history for any given experiment, which suggests that the conclusions presented in this work are robust. For instance, an example (experiment B_2) is exhibited in fig. 3 of K09.

We have considered several realizations whose relevant free parameters (e.g. initial orbital configuration and star formation efficiency) are summarized in Table 1. Our investigation mainly focuses on minor satellite mergers ($1/10 \leq$ mass ratio $\leq 1/4$), but we have also considered one major merger case (run D_1) with which to compare the results.

Table 1. Summary of merger simulations.

Run[a]	Mass ratio[b]	c_*^b	r_p [d]	Orbit[e]
A_1	1:10	0.01	8	Prograde
A_2	1:10	0.05	8	Prograde
A_3	1:10	0.1	8	Prograde
B_1	1:6	0.01	8	Prograde
B_2	1:6	0.05	8	Prograde
B_3	1:6	0.1	8	Prograde
B_4	1:6	0.05	6	Prograde
B_5	1:6	0.05	4	Prograde
B_6	1:6	0.05	2	Prograde
B_7	1:6	0.05	0	Prograde
B_8	1:6	0.05	8	Retrograde
C_1	1:4	0.01	8	Prograde
C_2	1:4	0.05	8	Prograde
C_3	1:4	0.1	8	Prograde
D_1	1:1	0.05	8	Prograde

[a]Name of run.
[b]Merger mass ratio (host:satellite).
[c]Star formation efficiency.
[d]Pericentric distance of orbit in kpc.
[e]Type of orbit.

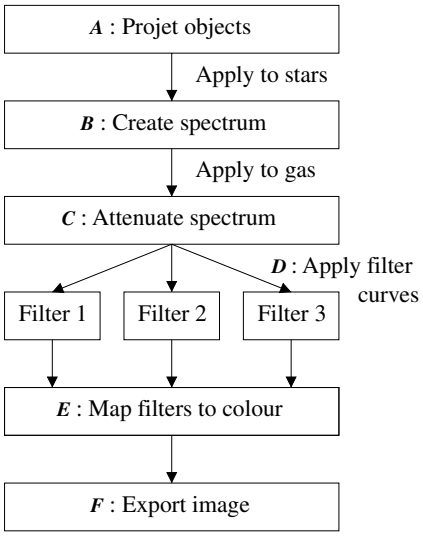

Figure 1. Flow diagram describing the pipeline for the rendering of telescope views of the objects in the simulation.

2.2 Modelling of WFC3 synthetic images

This section describes the numerical modelling that enables the rendering of physically realistic telescope views with user-definable filter curves for a simulated instrument. The rendering process is done using ray tracing of light emitted by the simulated objects. For such purpose, we have developed and used the ALICE code.[2]

The pipeline for the rendering of instrumental views is described in Fig. 1. First, the star and gas particles are projected on to a 2D array corresponding to the instrument's charge-couple device (CCD) pixels (A). This is done using a cosmological distance ladder, assuming a ΛCDM cosmology (e.g. Hogg 1999), with $H = 70\,\mathrm{km\,s^{-1}\,Mpc^{-1}}$, $\Omega_\mathrm{m} = 0.3$ and $\Omega_\Lambda = 0.7$ and a flat universe ($k = 0$). Next, we assign a stellar energy distribution and emission-line strength for various emission lines to each star particle (***B***), following Bruzual & Charlot (2003). To do this, we use an empirically determined age–metallicity relationship, derived from Prochaska et al. (2003). The spectra are frequency-shifted according to the Hubble and peculiar velocities relative to the simulated observer. Then the code runs the emission from the star particles and the absorption from the gas particles. Each of a given pixel's spectra and emission-line strengths is summed and attenuated (***C***) according to the gas column density (Calzetti et al. 2000, 2001). It is worth mentioning that the resolution of the simulations is not enough to resolve dense molecular gas or dust. Therefore, this may underestimate the total absorption which could affect the predicted UV emission. However, we do not think that the dust attenuation is very high since we showed in K09 that the (integrated) UV colours from this set of simulations reproduce the observed UV colours of the ETG populations extremely well. If we were systematically underestimating the dust content, then we would probably see quite a big mismatch between the UV red envelope predicted by the model simulations and the observed one. In the next step, these spectra are passed through a set of transmission filters (***D***). To do this, we linearly interpolate the spectra calculated with the given transmission curves. Finally, we produce flux maps corresponding to each transmission filter and emission line (***E***). We scale the fluxes to the minimum flux detectable by the instrument in each wavelength.

Table 2. UVIS filter characteristics.

F225W	F487N	F555W
0.2–0.275 μm	0.48–0.49 μm	0.45–0.7 μm

Table 3. IR filter characteristics.

F110W	F160W
0.9–1.4 μm	1.4–1.7 μm

For the purposes of this work, the instrument parameters were taken from the WFC3 instrument. For instance, we have considered five filters: two from the near-infrared (NIR) field, *J* (F110W) and *H* (F160W), and three from the UV/optical field, NUV (F225W), the narrow-band Hβ (F487N) and *V* (F555W) (see Tables 2 and 3 for the associated wavelength bands). The UV colours are particularly suitable to detect young stellar populations inside interacting galaxies (see, for instance, Hibbard et al. 2005) and remains largely unaffected by the age–metallicity degeneracy (Worthey 1994) while the NIR spectral window traces primarily the old stellar populations.

Synthetic 2D images have been produced assuming luminosity distances of $D = 100$ and $D = 20\,\mathrm{Mpc}$ corresponding to $z \sim 0.023$ and $z \sim 0.005$, respectively, and according to the cosmological parameters considered. An exposure time, $t = 3600\,\mathrm{s}$, was used for each of the broad-band filters, while $t = 7200\,\mathrm{s}$ was used for the narrow-band Hβ filter. We have assumed that each image is made up of 10 exposures in order to calculate an appropriate readout noise. The FOV of our synthetic images match those of the WFC3 detectors, namely $162 \times 162\,\mathrm{arcsec^2}$ for UVIS images and $133 \times 133\,\mathrm{arcsec^2}$ for IR images. All the images have been convolved with an appropriate *HST* point-spread function (PSF), derived using the TINYTIM[3] software package (Krist & Hook 2004). Finally, an appropriate sky background, Poisson noise and readout noise have been added to each of the filtered images. Although generated at the full resolution of the UVIS instrument (4096 × 4096 pixels),

[2]www-astro.physics.ox.ac.uk/∼samgeen/alice/index.html

[3]www.stsci.edu/software/tinytim

the UVIS images presented in this paper have been re-binned to a resolution of 1024 × 1024.

3 RESULTS

3.1 Evolution of the star formation rates

In Figs 2 and 3, we present the time evolution of the SFRs derived from experiments described in the previous section. In each case, we have let the system evolve until $t = 4.0$ Gyr from the beginning of the simulation, which corresponds to $\sim 30\, t_{\rm dyn}$ where $t_{\rm dyn} = [r_{\rm vir}^3/GM_{\rm host}(r_{\rm vir})]^{1/2}$ is the dynamical time-scale at the virial radius of the host elliptical galaxy. In our models, $r_{\rm vir} \approx 13.5$ kpc and $M_{\rm host}(r_{\rm vir}) \approx 3.12 \times 10^{10}\, {\rm M}_{\odot}$ which lead to $t_{\rm dyn} \sim 1.3 \times 10^8$ yr. This value is consistent with observationally determined dynamical times from SDSS parameters (petroRad, photometric stellar masses, etc.) that are around 0.1 Gyr for ETGs. Young (2002) has also studied interferometric images of CO emission in five elliptical galaxies and derived some dynamical time-scales for gas discs which are between 0.07 and 0.2 Gyr.

We first note the presence of peaks in the evolution of the SFRs that are associated with recent pericentric passages of the satellite. Indeed, at these specific times, an important fraction of available gas is consumed in starbursts due to the increase in the gas density during the interaction. The last peak in the SFRs is due to the final plunge of the satellite remnant. This behaviour can be clearly seen in Fig. 2, where the evolution of the SFR derived from experiment B_2 is plotted in parallel with the variation of the radial distance D of the bound part of the satellite remnant (with respect to the host galaxy centre). We can observe that each SFR peak is preceded by a minimum in D. Physically, these features arise due to tidal forces that induce instabilities in the satellite disc, resulting in loss of angular momentum via dynamical friction and infall to the centre.

The presence of several peaks in the SFR evolution seems to be a general trend in the case of minor merger events (mass ratio of $\leq$1:4). A similar evolution is obtained even while assuming different star formation efficiencies or different initial orbital configurations (see Fig. 2). We also find similar behaviour for experiments B_5 and B_6 (e.g. for a mass ratio of 1:6 and $r_{\rm p} = 4$ and 2 kpc, respectively). For reasons of clarity, we have omitted showing their evolution in Fig. 2.

However, the result is different for a major merger event. The right-hand panel of Fig. 3 indicates that only two peaks are

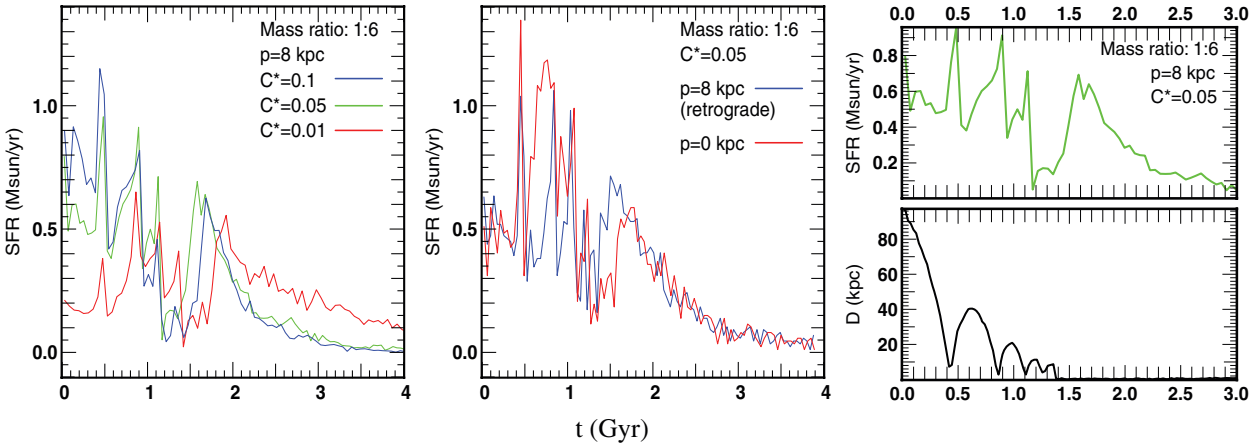

Figure 2. The variations of the SFRs derived from 1:6 merger mass ratio scenarios. The left-hand panel shows the evolution of SFRs for a fixed pericentric distance ($r_{\rm p} = 8$ kpc) but with different star formation efficiency c_* values. The middle panel presents SFRs derived from experiments B_8 (retrograde orbit) and B_7 (edge-on parabolic merger). In the right-hand panel, we have plotted in parallel the SFR derived from experiment B_2 and the evolution of the radial distance of the most bound part of the satellite.

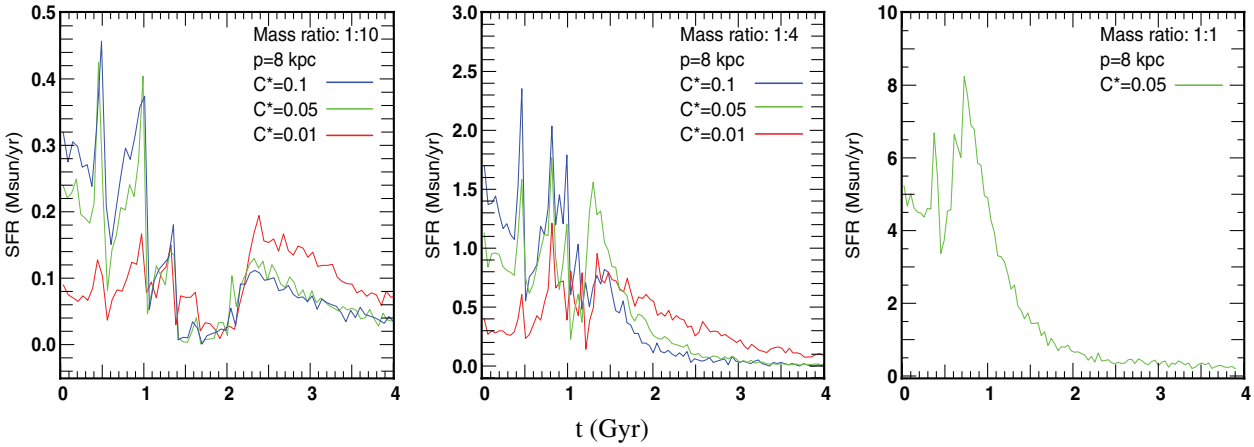

Figure 3. The variations of the SFRs derived from 1:10 (left-hand panel), 1:4 (middle panel) and 1:1 (right-hand panel) merger mass ratio scenarios.

observed. In fact, the time-scale of the merging process decreases as the mass ratio of the system increases. The time delays between the final plunge and the first peak are ∼1.75, ∼1.25 and ∼1. Gyr for progenitor mass ratios of 1:10, 1:6 and 1:4, respectively. This is mainly due to the fact that the satellite galaxy gradually loses its energy and angular momentum under the action of dynamical friction and finally sinks to the centre of the host galaxy. This dynamical friction operates more slowly for minor merger events (see, for instance, Binney & Tremaine 2008). The ages of the individual minibursts are determined by the orbit and its dynamical evolution.

We also note that if the star formation efficiency c_* is low, a larger reservoir of gas remains at the time of the final plunge. This can sustain star formation in the remnant for a longer time as is clearly suggested in Fig. 2. This result confirms both earlier studies (Larson 1974) and previous work based on merger simulations which show that gas can settle in a self-gravitating central disc which may feed a central black hole (Mihos & Hernquist 1996; Barnes 2002).

To finish, it should be pointed out that any initial transient starbursts and numerous fluctuations seen in the SFRs before the first pericentric distance may result from non-equilibrium initial conditions. Indeed, such starbursts can happen at the beginning of the simulation since all stars are unaffected by feedback and then most of them may be eligible to form stars. The numerous fluctuations seen in SFRs are also explained by the fact that a short period is needed for Type II SNe to be effective in order to regulate the star formation in the galaxy.

3.2 Evolution of the spatial distribution of stars

In this section, we focus on the evolution of the spatial distribution of stars. In our models, stars can be divided into three distinct groups: those that initially belong to the elliptical galaxy (E_*), those that were present in the disc before the merger (D_*) and finally the new stars which have formed during the merger process (N_*). We are particularly interested in the latter stars. It is worth mentioning that we use the same initial age distribution as in K09, i.e. we assume that the elliptical is composed of old stars of an age of 9 Gyr whereas the mean age of the stellar population in the initial disc is 5 Gyr. The motivation of such choices is described in K09.

Fig. 4 shows the evolution of the projected distribution (face-on) of all stars in experiment B_2. After 1.5 Gyr, we note that the remnant satellite progressively forms a so-called shell galaxy, in agreement with previous numerical studies (Quinn 1984; Dupraz & Combes 1986 ; Hernquist & Quinn 1988; Hernquist & Spergel 1992; Hernquist & Mihos 1995). The age of all stars is also plotted with a colour coding. At large radius, the shell structure is mainly composed of a fossil stellar population of accreted stars D_*. Such trends are in good agreement with observations of massive ETGs (see, for instance, Clemens et al. 2009b). This is mainly due to the dissipationless process and angular momentum conservation during the merger. The newly formed stars N_* are generally formed in the central part of the satellite remnant where the density is higher. On the contrary, the gaseous component of the satellite falls dissipatively into the potential well of the host galaxy and, after the final plunge, fuels rapid star formation. This latter phase is clearly active in the inner part of the system ($\leq$3 kpc), and after 2 Gyr it may be possible to measure a gradient in the age of the newly formed stars within ∼40 kpc, as suggested by Fig. 5. Since these new stars may have a higher metallicity than the host old ones, the presence of a metallicity gradient is also expected, in agreement with observations (Clemens et al. 2009b).

3.3 Size evolution of wet merger remnants

Simple arguments based on the virial theorem allow us to calculate the size evolution of the collisionless component of the merger remnant (e.g. Bezanson et al. 2009; Naab, Johansson & Ostriker 2009). Assuming that the individual stellar components of the galaxies are in virial equilibrium,

$$E_i = -\frac{f}{2}\frac{GM_i^2}{r_i}. \quad (1)$$

The factor f depends on the individual functional form of the profile and is close to $f = 0.5$ in the case of de Vaucouleurs and exponential profiles. The radius r is the half-mass radius of the galaxy and M its stellar mass. The merging galaxies are set up to be on parabolic orbits with $E_{\rm orb} = 0$, which allows us to write down the internal energy of the remnant assuming energy conservation as

$$E_{\rm rem} = E_1 + E_2 + E_{\rm orb} = -\frac{f}{2}G\left[\frac{M_1^2}{r_1} + \frac{M_2^2}{r_2}\right]. \quad (2)$$

Assuming that the remnant will settle down in virial equilibrium, basic manipulations of equation (2) lead to

$$\frac{(M_1 + M_2)^2}{r_{\rm rem}} = \frac{M_1^2}{r_1} + \frac{M_2^2}{r_2}. \quad (3)$$

In the following, we investigate the merger remnants and characterize the deviations from this simple virial argument based on the rate of dissipation and star formation occurring during the merger. For this purpose, we focus again on experiment B_2 which can be considered as a typical minor merger scenario. In this case, we obtain $r_{\rm rem} \sim 5.67$ kpc.

From the simulation, the half-mass radius $R_{\rm e}$ at a given time is defined to be the radius of the circle containing half of the projected stellar mass. We have also studied the evolution of effective radii $R_{\rm e}^V$ and $R_{\rm e}^H$ from V and H bands, respectively. $R_{\rm e}^V$ and $R_{\rm e}^H$ are defined to be the radii containing half of the projected flux in each specific band. In order to take into account the effects of the viewing angle, we have considered 100 different lines of sight chosen randomly and derived the mean value of $R_{\rm e}$, $R_{\rm e}^V$ and $R_{\rm e}^H$.

Fig. 6 shows the evolution of $R_{\rm e}$, $R_{\rm e}^V$ and $R_{\rm e}^H$ after the final plunge for experiment B_2. The evolution of $R_{\rm e}$ tends to a constant value ($R_{\rm e} \sim 5.05$ kpc) which is lower than the predicted value $r_{\rm rem} \sim 5.67$ kpc. This result is in agreement with the study of Covington et al. (2008) who show that the model systematically overpredicts the radii of remnants and using a wide range of merger simulations which account for dissipative energy losses and star formation.

The evolution of $R_{\rm e}^V$ is different and presents two phases. First, a rapid decrease just after the final plunge ($t \sim 1.6$ Gyr) which continues for ∼0.5 Gyr. This period corresponds to a phase of high star formation induced by the final plunge as shown in Fig. 2. The newly formed stars, mainly located in the central region, have a significant contribution of the total flux in the V band leading to the reduction in $R_{\rm e}^V$. In the second phase, beginning at $t \sim 2.25$ Gyr, $R_{\rm e}^V$ increases due to the fact that the stellar population becomes progressively older. Indeed, such behaviour can be clearly seen in the lower panel of Fig. 6 where we have plotted the evolution of the half-mass radius for each stellar component E_*, D_* and N_*. The half-mass radius of the host elliptical galaxy tends to a constant value (∼4.2 kpc) which is actually very close to but lower than the initial value (4.29 kpc) and probably due to the adiabatic contraction induced by the infall of the satellite at the centre. The half-mass radius of stars of the initial disc D_* also tends to a constant value (∼11.5 kpc), which is quite high but explained again by the dissipationless process and angular

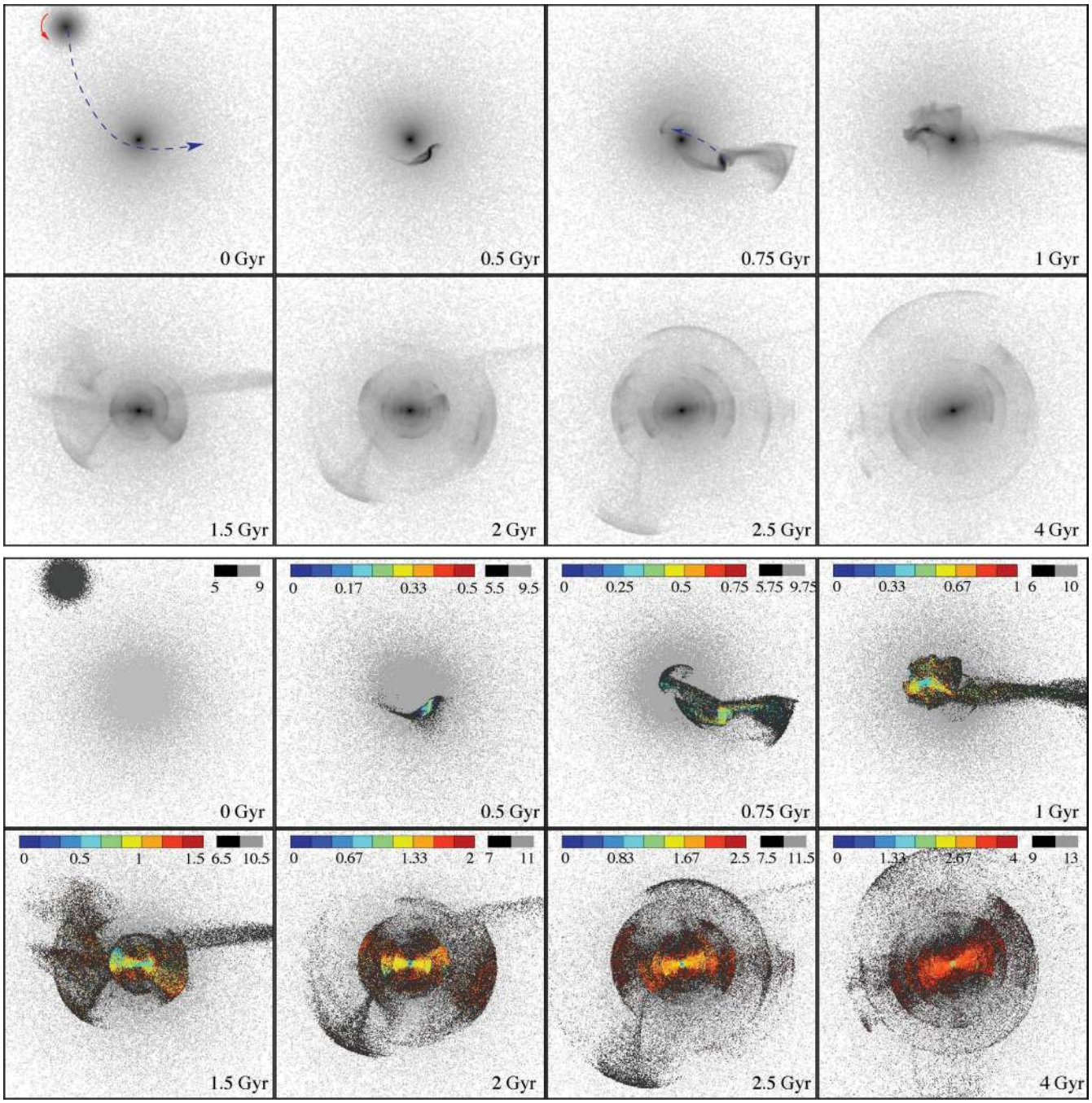

Figure 4. The evolution of the projected spatial distribution of stars (face-on) from experiment B_2. Lines 1 and 2 show all stars in grey-scale. In the upper panels, the dashed blue lines indicate the trajectories of the satellite while the red arrows shows the initial spin of the spiral galaxy. Lines 3 and 4 represent the stellar ages of the newly formed stars (in Gyr) at the same specific times. Each square is $100 \times 100\,\mathrm{kpc}^2$ in size.

momentum conservation during the merger. Finally, the half-mass radius for the newly formed stars N_* is rapidly decreasing until $t \sim 3.0$ Gyr due to the high star formation induced after the final plunge. After this time, the increase observed in the evolution of R_e^V results from the ageing of the stellar population N_*.

The evolution of R_e^H follows the same trend, though the decrease after the final plunge is less pronounced but continues for a longer time ($\sim$2.0 Gyr). The value of R_e^H is close to R_e values but still smaller. It is expected that both R_e^V and R_e^H asymptotically tend to the value of R_e at late time. We infer that because of even modest amounts of star formation, the half-mass radius differs significantly from the half-light radius especially in the V band. The observed half-light radius is expected to be smaller than the half-mass radius.

3.4 Evolution of WFC3 bands

In order to produce synthetic images, we have assumed our galaxy system to be in the local universe. Such a choice is motivated by the fact that up to two-thirds of nearby ETGs contain shells and ripples (see, for instance, Malin & Carter 1983; van Dokkum 2005), and these fine structures and disturbed morphologies often coincide with signatures of recent star formation (e.g. Schweizer et al. 1990;

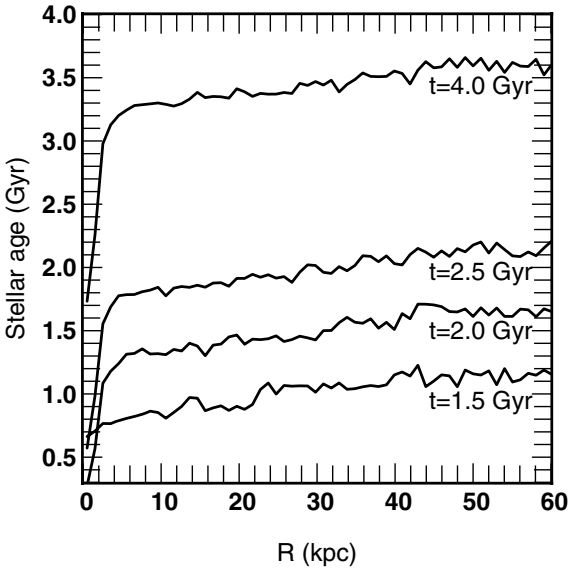

Figure 5. Evolution of the distribution of ages of newly formed stars (face-on) at different times from the beginning of the simulation for experiment B_2.

Schweizer & Seitzer 1992). It is then particularly interesting to try to characterize this spatially resolved fine structure whose detection is possible only in our local neighbourhood. For instance, using N-body simulations, Feldmann, Mayer & Carollo (2008) have shown that this broad tidal feature cannot be reproduced by an equal-mass dissipationless merger but is well explained by the accretion of disc-dominated galaxies. Moreover, minor mergers are expected to be more common than major mergers at low redshifts (Khochfar & Silk 2006; Genel et al. 2008; Khochfar & Silk 2009) and such statements support our choice of merger mass ratio values.

We start our investigation with experiment B_2. The galaxy pair is supposed to be at a redshift $z \sim 0.023$ (or equivalently at a luminosity distance of $D = 100$ Mpc) in order to facilitate comparisons with future observational data. In the following, the magnitude units given as measures of spectral flux are $W \cdot m^{-2}$, and in all synthetic images, we use a logarithmic scale.

In Fig. 7, we present the grid map derived by our numerical modelling through the J and H bands. It appears that it is possible to resolve the host elliptical galaxy and the satellite remnant, in particular the shell structure which is mainly composed of old stars. However, this latter tends to disappear at $t = 4.0$ Gyr. We also note that there are no significant differences between J and H bands. Fig. 8 shows the evolution of derived synthetic images from NUV, Hβ and V bands. The ongoing star formation regions can be clearly followed through the three filters. In particular, after the final plunge, ongoing star formation located at the centre of the galaxy can be clearly observed. In fact, when comparing with Fig. 4, only stars with ages of $\leq$0.5 Gyr can be identified. Thus, the combination of IR and UVIS images allows us to separate different stellar populations and then distinguish the most bound part of the satellite remnant, composed of young stars, from the host galaxy, composed of older stars. This combination also gives useful clues to the formation of ETGs: while the shell structure revealed in IR images supports a past merger scenario, evidence or not of the presence of young stars in UVIS images brings additional constraints on the wetness/dryness of the merger.

The same study has been performed for objects assumed to be at $z \sim 0.005$ ($D = 20$ Mpc). In this case, only the inner part is imaged due to the instrument FOV, as shown in Figs 9 and 10. The evidence of recent star formation is again clearly visible especially in the NUV band after the final plunge ($t \geq 1.5$ Gyr). Some structures can also be distinguished around the central part and represent signatures of a recent merger event.

We have also studied how the free parameters (star formation efficiency and initial mass ratio) affect our results. For instance, Fig. 11 shows the evolution of synthetic images from the J and NUV bands in experiment B_1. In this case, although the star formation efficiency is lower, the satellite remnant can also be identified in the NUV band. In the J band, the shell structure is less pronounced.

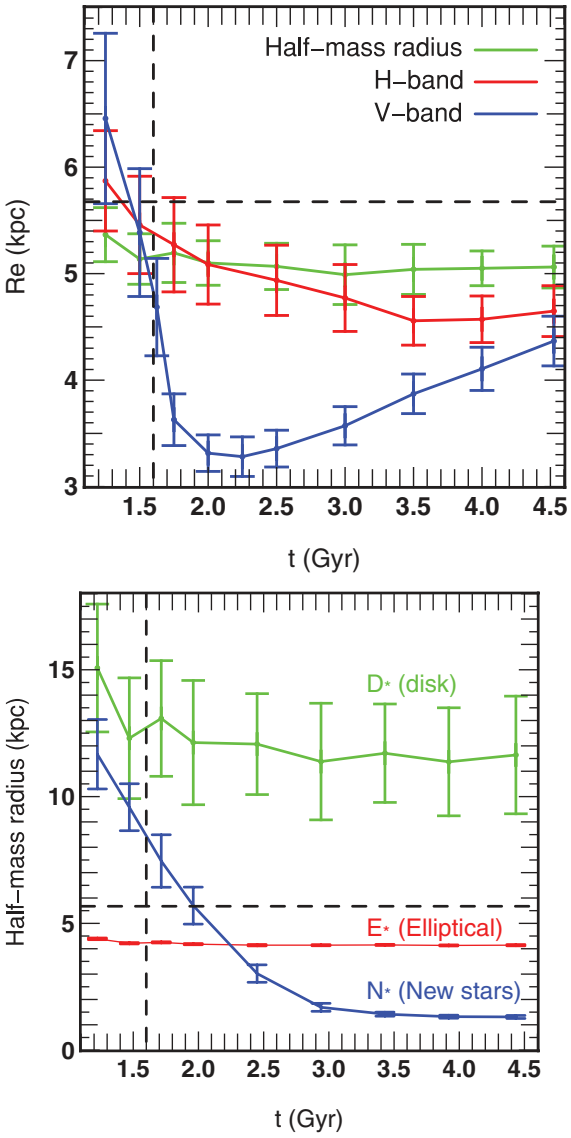

Figure 6. The upper panel shows the evolution of the half-mass radius (green line) and effective radius from V (blue) and H (red) bands for experiment B_2. In the lower panel, we show the evolution of the half-mass radius for each stellar component: stars that initially belong to the host elliptical galaxy (E_*, red line), those that were present in the disc before the merger (D_*, green line) and the new stars which have been formed during the merger process (N_*, blue line). In each panel, the horizontal dashed line is the predicted half-mass radius value after the merger from arguments based on the virial theorem whereas the vertical dashed line is the epoch of the final plunge.

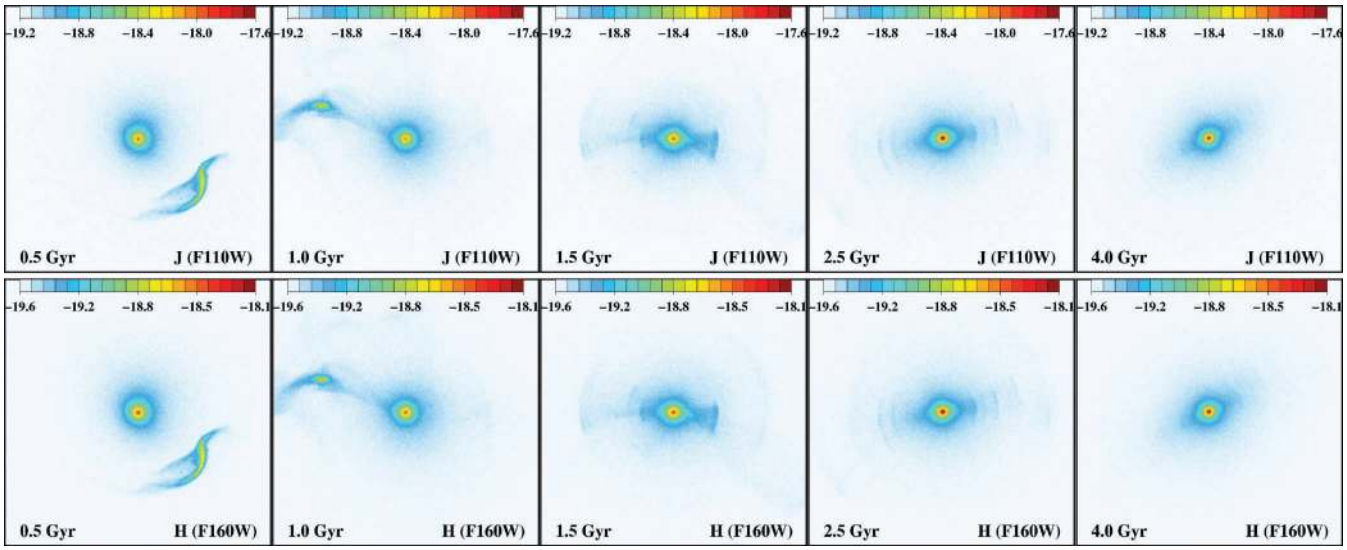

Figure 7. The evolution of synthetic images from experiment B_2 through J (first line) and H bands (second line) assuming the observed system at $z \sim 0.023$. The images have been Gaussian smoothed with a sigma of 2 pixels.

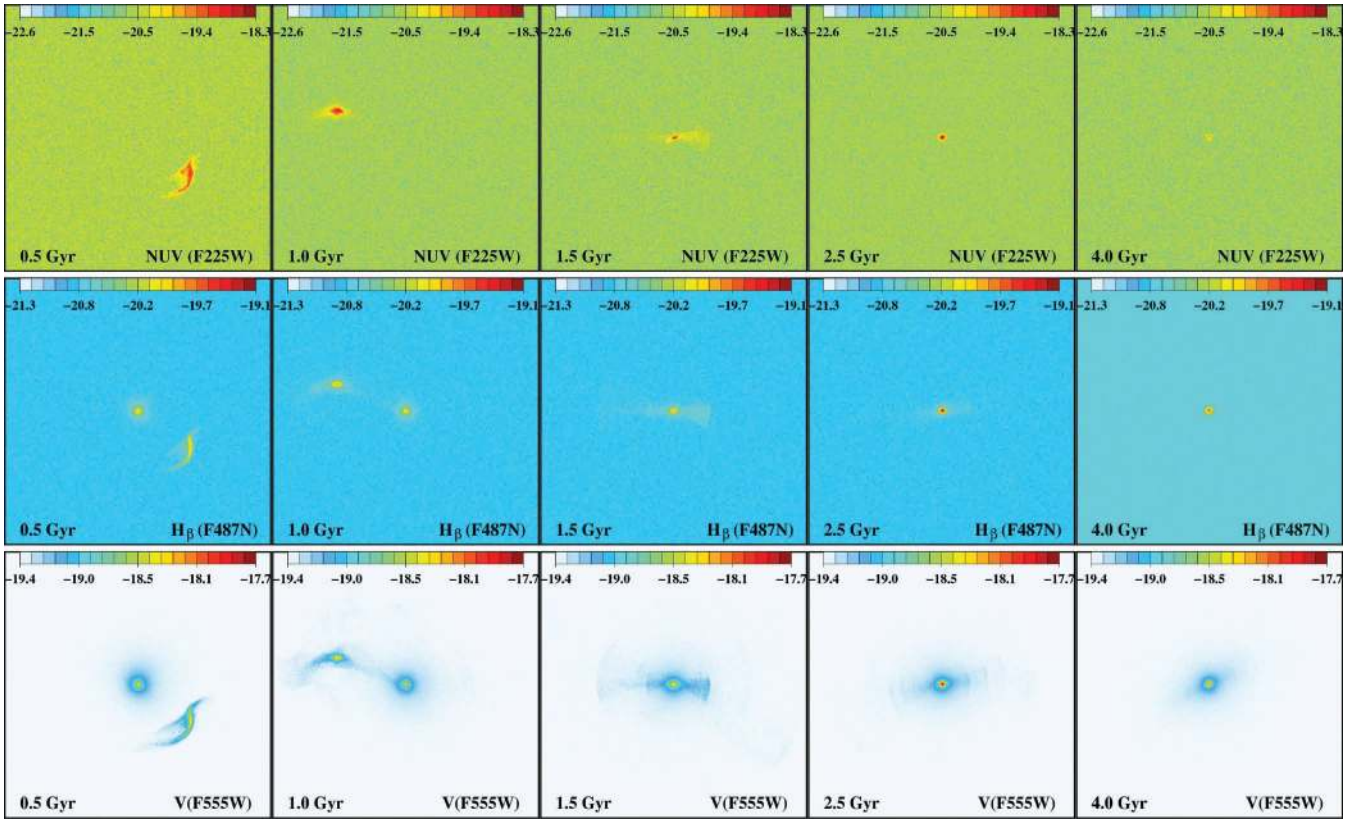

Figure 8. The evolution of synthetic images from experiment B_2 through NUV (first line), Hβ (second line) and V (third line) bands assuming the observed system at $z \sim 0.023$.

Comparison with mass ratios of 1:4 and 1:10 presents similar conclusions although the structures are better resolved in the case of the 1:4 mass ratio due to the higher star formation induced during the merger (see Figs 12 and 13). For instance, maximum values in the NUV band between 1:4 and 1:10 merger mass ratios differ by up to an order of magnitude while they are comparable in the H band. However, simulations with the 1:4 merger mass ratio should be regarded as a limiting case, since it is close to the major merger scenario.

4 DISCUSSION

The formation of ETGs remains a major unresolved problem in astrophysics, and in particular their star formation history is known

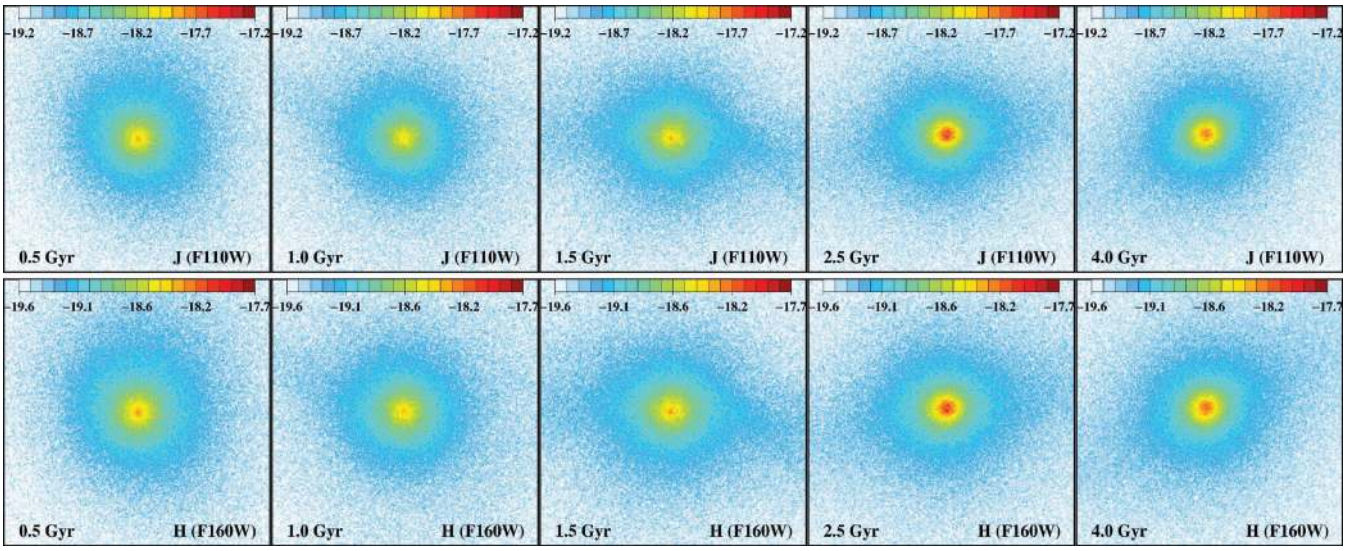

Figure 9. The evolution of synthetic images from experiment B_2 through J (first line) and H (second line) bands assuming the observed system at $z \sim 0.005$.

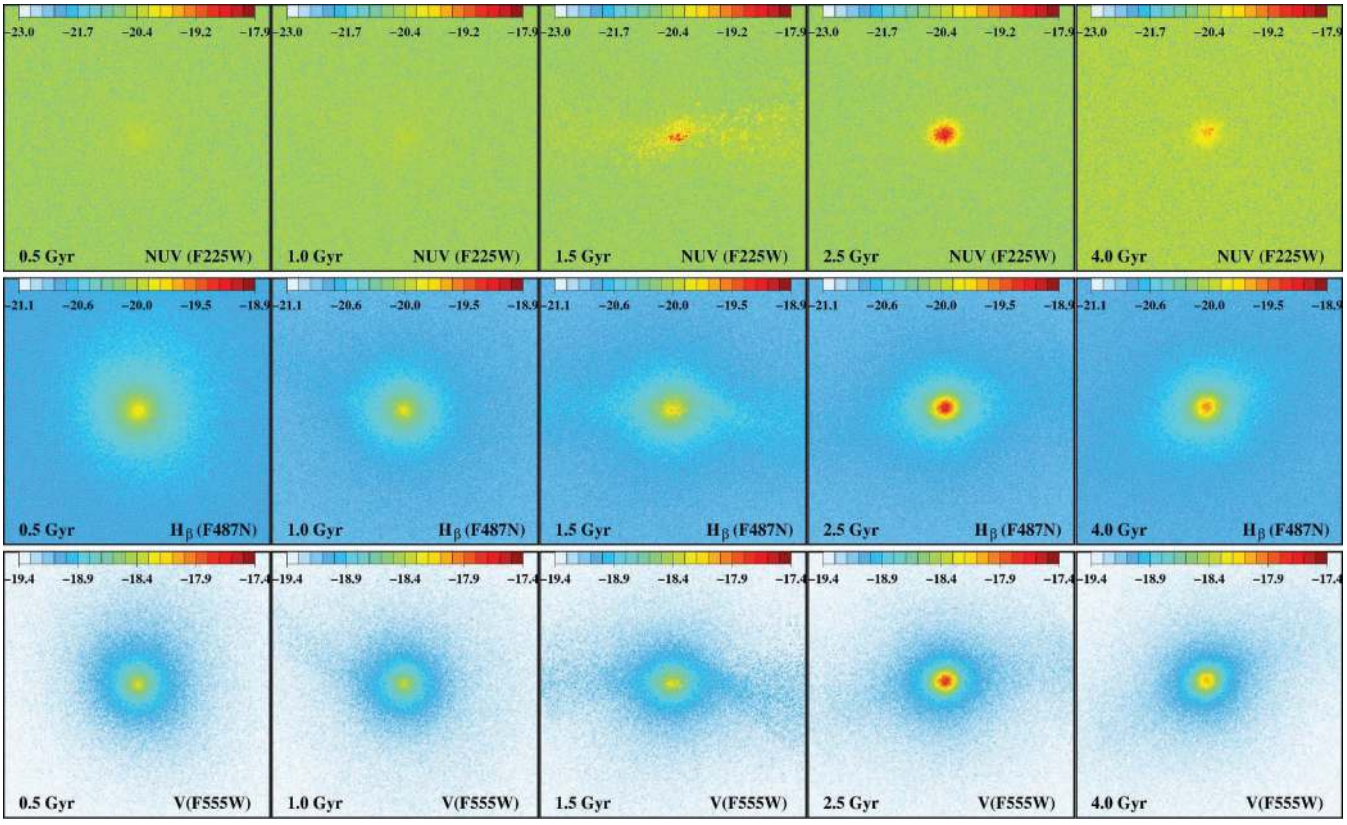

Figure 10. The evolution of synthetic images from experiment B_2 through NUV (first line), Hβ (second line) and V (third line) bands assuming the observed system at $z \sim 0.005$.

to be more complex than that of a single population model. Studies of nearby galaxy populations can provide useful clues to resolving this problem, by setting tight constraints on the level of the most recent star formation activity. In this paper, we have used idealized hydrodynamical simulations, including a standard star formation prescription, to study the minor merger process between an elliptical and a spiral galaxy which is expected to be the dominant channel in terms of the morphology of the merging galaxies (Khochfar & Burkert 2003). There is now observational evidence that massive ETGs may have undergone not more than one major merger since $z \sim 0.7$ (Bell et al. 2006; McIntosh et al. 2008). Such results are supported by theoretical evidence that massive haloes ($\geq 10^{11}$ M$_\odot$) experience only one major merger between $z = 2$ and $z = 0$, while minor mergers are much more common (Khochfar & Silk 2006, 2009; Genel et al. 2008). We use idealized simulations in this work for two main reasons. First, it allows us to reach a high-mass

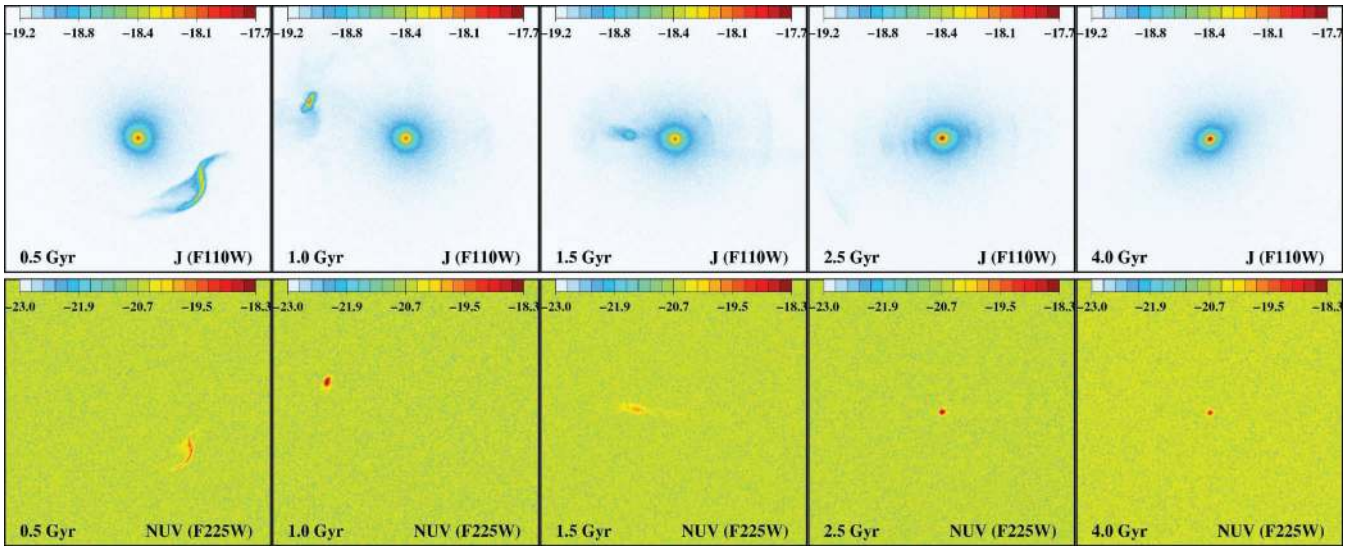

Figure 11. The evolution of synthetic images from experiment B_1 (mass ratio of 1:6 and $c_* = 0.01$) through J (first line) and NUV (second line) bands assuming the observed system at $z \sim 0.023$.

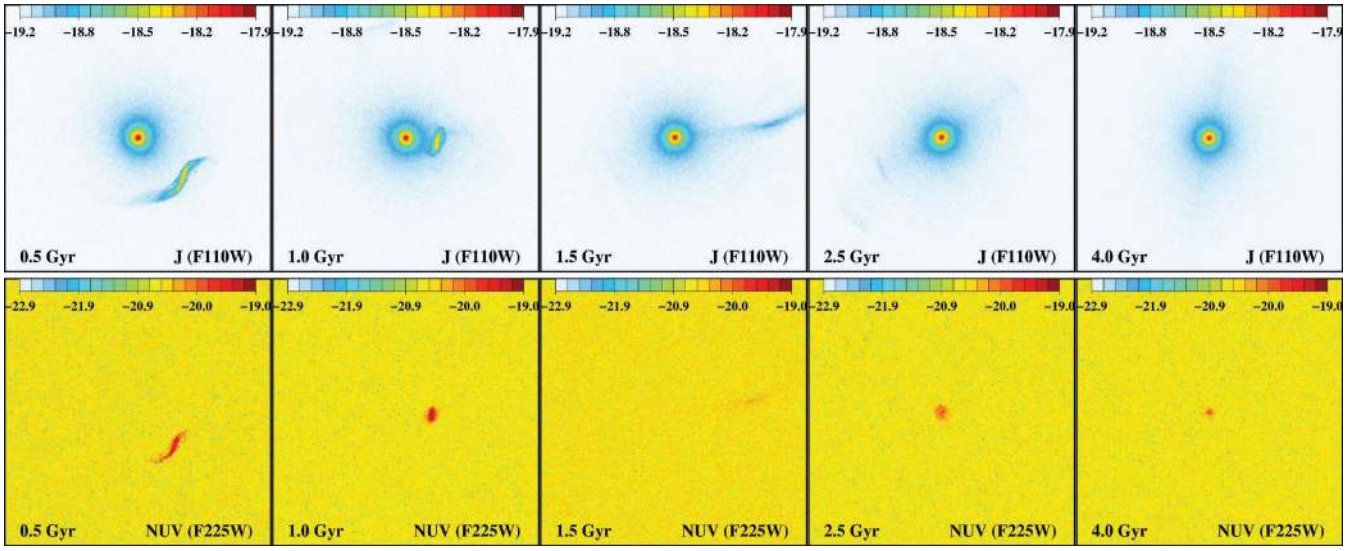

Figure 12. The evolution of synthetic images from experiment A_2 (mass ratio of 1:10 and $c_* = 0.05$) through J (first line) and NUV (second line) bands assuming the observed system at $z \sim 0.023$.

resolution ($\sim 10^{4-5}$ $M_\odot$) with reasonable computational costs compared to cosmological simulations. Secondly, it permits us to consider a wide range of free parameters (including star formation efficiencies and initial orbital parameters) and to study how the results change accordingly.

We have generated 15 experiments by considering different merger mass ratios (1:10, 1:6, 1:4 and 1:1) and three star formation efficiencies ($c_* = 0.01$, 0.05 and 0.1). We find that the satellite is progressively disrupted by tidal torques and the star formation induced by the merger process shows several peaks in its evolution, associated with the passage of the remnant at decreasing pericentric distances. The satellite remnant progressively forms a shell structure within the host galaxy, which is composed of old stars at large radii and is explained by the fact that the stellar accretion and ensuing relaxation occurs via dissipationless mechanisms. On the contrary, the centre is dominated by the newly formed stars due to the infall of the gas to the centre in a dissipative process. A positive radial age gradient is clearly seen and remains constant in time. All of these results are consistent with the conclusions of observational studies of massive ETGs (see, for instance, Clemens et al. 2009b).

These typical shell structures are of particular interest as a means of characterizing the last merger experienced by the host galaxy, i.e. the mass ratio, dryness or orbital configuration. For instance, recently Canalizo et al. (2007) have tried to set constraints on the age of the plausible merger responsible for shell structures observed in a quasar host galaxy from *HST*/Advanced Camera for Surveys (ACS). By using N-body simulations, they found that the merger occurred a few hundred Myr to $\sim$2 Gyr ago when matching the observed and simulated outermost shell and causal connection with the quasar activity. But the accurate estimation of the age of the merger proves to be a very hard task due to the high number of orbital parameters, even when combining dynamical and photometric properties of the galaxy. For instance, Di Matteo et al. (2007) investigated the evolution of star formation efficiency in galaxy interactions and mergers

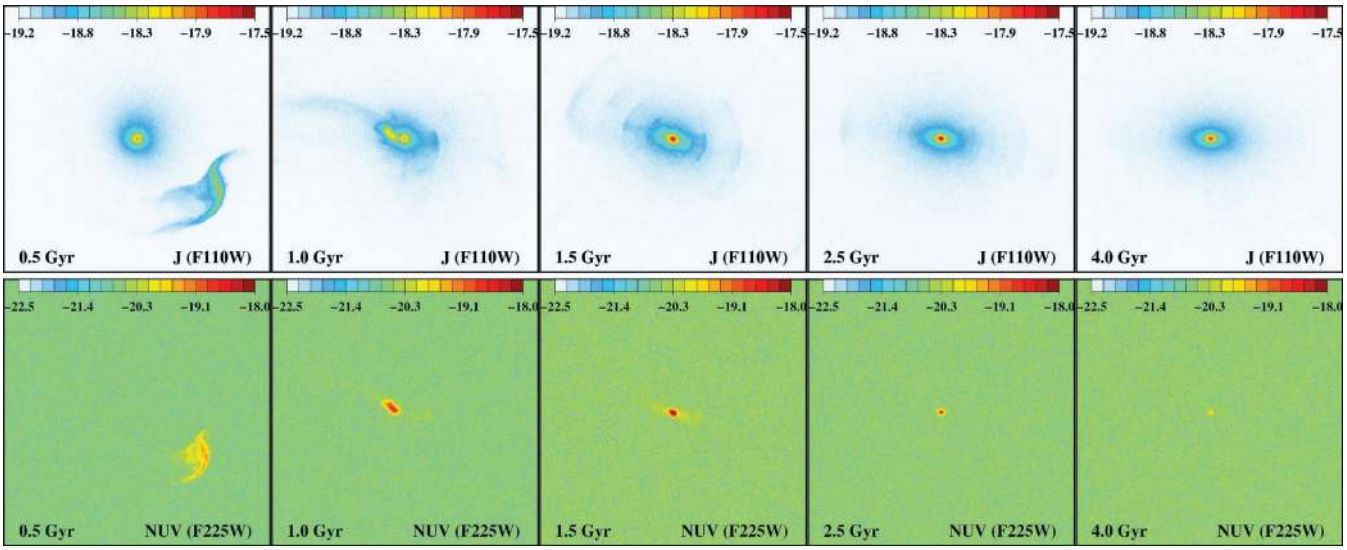

Figure 13. The evolution of synthetic images from experiment C_2 (mass ratio of 1:4 and $c_* = 0.05$) through J (first line) and NUV (second line) bands assuming the observed system at $z \sim 0.023$.

using numerical simulations and found that retrograde orbits or high pericentric distances favour the enhancement of the star formation. Such degeneracy may be difficult to deal with.

Our main result is to demonstrate that colour information provides an important additional constraint via the induced star formation that together with the associated morphology provides further and important insights into the merger parameters. In particular, future observations especially with the resolution and NUV power of WFC3 will open new vistas on star formation histories of ETGs. We have derived realistic synthetic images through J, H, NUV, Hβ and V filters that can be compared with future WFC3 observations. Comparison of synthetic maps in the NUV and J bands for different merger mass ratios and star formation efficiencies gives similar results: evidence of recent star formation can be clearly detected before and after the final plunge, especially in the NUV band.

Our study does not include AGN feedback. We will consider this in a future paper. Here we note that while such a mechanism is supposed to play an important role in the early phases of the spheroid star formation, its role in the late phase is still poorly known. As suggested by our results, the infall of the gas at the final plunge can settle in a self-gravitating central disc which may feed a central black hole. For instance, N-body simulations including feedback from black hole accretion indicate that the quasar activity is coincident with the coalescence of the nuclei and eliminate all star formation afterwards (Springel et al. 2005). This will probably lead to a reduction of the total flux in the UVIS bands.

In summary, minor mergers seem to play a fundamental role in the late phases of ETG evolution. Minors mergers may be the principal mechanism behind the large UV scatter and associated low-level recent star formation observed in ETGs in the nearby universe (K09). In general, we find composite populations contributing to the SFR which persists for 2–3 Gyr, corresponding to several orbital times. Minor mergers naturally lead to star formation that is extended over a much longer period than for the single population starburst. The limiting case of major mergers results in much shorter star formation time-scales. Size evolution is another natural consequence of the minor merger model. The considerable amount of dissipation and central star formation reduces the apparent half-light radius of the merger remnant compared to its half-mass radius (see Fig. 6), thus indicating that size determinations based on rest-band magnitudes sensitive to star formation will clearly underestimate sizes by factors of 1.2–1.6 for a few Gyr after the merger. Taking our results at face value and considering that the frequency of gas-rich minor mergers is larger at earlier times, the size evolution of elliptical galaxies from high to low redshift could be milder than assumed so far.

To conclude, this work shows that minor mergers induce amounts of star formation in ETGs which can be measured through UV bands. WFC3 represents the best instrument to study these minor merger events because it has a matching UV and optical FOV and gives the resolution to see young substructures (which would not be possible with *GALEX* for instance). The previous ACS/High Resolution Channel (HRC) UV detectors had a tiny FOV, so it was not possible to study a galaxy up to 1 effective radius because one would get the whole galaxy in the optical image and only a fraction of its core using the UV. With WFC3, it is now possible to map the entire galaxy in both the UV and optical making it possible for the first time to perform spatially resolved star formation histories in ETGs at low redshift using the UV. Moreover, the ability to see the young substructures is important because it rules out UV flux from old sources such as horizontal branch stars (which would follow the optical light profile).

ACKNOWLEDGMENTS

SP acknowledges support from 'Agence Nationale de la Recherche' ANR-08-BLAN-0222-02, RMC and SG from the STFC and SK through an Imperial College Junior Research Fellowship, a Research Fellowship from the Royal Commission for the Exhibition of 1851 and a Senior Research Fellowship at Worcester College, University of Oxford. We warmly thank the referee for his useful comments that helped to improve the text of this paper.

REFERENCES

Arimoto N., Yoshii Y., 1987, A&A, 173, 23
Barnes J. E., 2002, MNRAS, 333, 481
Bell E. F. et al., 2006, ApJ, 640, 241

Bezanson R., van Dokkum P. G., Tal T., Marchesini D., Kriek M., Franx M., Coppi P., 2009, ApJ, 697, 1290
Binney J., Tremaine S., 2008, in Binney J., Tremaine S., eds, Galactic Dynamics, 2nd edn. Princeton Univ. Press, Princeton, NJ, ISBN 978-0-691-13026-2 (HB)
Blumenthal G. R., Faber S. M., Primack J. R., Rees M. J., 1984, Nat, 311, 517
Bressan A. et al., 2006, ApJ, 639, L55
Bruzual G., Charlot S., 2003, MNRAS, 344, 1000
Calzetti D., 2001, PASP, 113, 1449
Calzetti D., Armus L., Bohlin R. C., Kinney A. L., Koornneef J., Storchi-Bergmann T., 2000, ApJ, 533, 682
Canalizo G., Bennert N., Jungwiert B., Stockton A., Schweizer F., Lacy M., Peng C., 2007, ApJ, 669, 801
Cimatti A., 2009, AIP Conf. Ser. Vol. 1111, Probing Stellar Populations Out to the Distant Universe: Cefalu. AIP, Melville, NY, p. 191
Cimatti A., Daddi E., Renzini A., 2006, A&A, 453, L29
Clemens M. S., Bressan A., Panuzzo P., Rampazzo R., Silva L., Buson L., Granato G. L., 2009a, MNRAS, 392, 982
Clemens M. S., Bressan A., Nikolic B., Rampazzo R., 2009b, MNRAS, 392, L35
Colless M., Burstein D., Davies R. L., McMahan R. K., Saglia R. P., Wegner G., 1999, MNRAS, 303, 813
Covington M., Dekel A., Cox T. J., Jonsson P., Primack J. R., 2008, MNRAS, 384, 94
Di Matteo P., Combes F., Melchior A.-L., Semelin B., 2007, A&A, 468, 61
Djorgovski S., Davis M., 1987, ApJ, 313, 59
Dupraz C., Combes F., 1986, A&A, 166, 53
Eggen O. J., Lynden Bell D., Sandage A. R., 1962, ApJ, 136, 748
Feldmann R., Mayer L., Carollo C. M., 2008, ApJ, 684, 1062
Fukugita M. et al., 2007, AJ, 134, 579
Genel S. et al., 2008, ApJ, 688, 789
Glazebrook K. et al., 2004, Nat 430, 181
Goudfrooij P., Hansen L., Jorgensen H. E., Norgaard-Nielsen H. U., 1994, A&AS, 105, 341
Hernquist L., Mihos J. C., 1995, ApJ, 448, 41
Hernquist L., Quinn P. J., 1988, ApJ, 331, 682
Hernquist L., Spergel D. N., 1992, ApJ, 399, L117
Hibbard J. E. et al., 2005, ApJ, 619, L87
Hogg D. W., 1999, preprint (astro-ph/9905116)
Jiang G., Kochanek C. S., 2007, ApJ, 671, 1568
Jorgensen I., Franx M., Kjaergaard P., 1996, MNRAS, 280, 167
Kannappan S. J., 2004, ApJ, 611, L89
Kauffmann G., White S. D. M., Guiderdoni B., 1993, MNRAS, 264, 201
Kaviraj S. et al., 2007, ApJS, 173, 619
Kaviraj S., Peirani S., Khochfar S., Silk J., Kay S., 2009, MNRAS, 394, 1713 (K09)
Kaviraj S., Tan K.-M., Ellis R. S., Silk J., 2010, preprint (arXiv:1001.2141)
Khochfar S., Burkert A., 2003, ApJ, 597, L117
Khochfar S., Burkert A., 2006, A&A, 445, 403
Khochfar S., Silk A., 2006, MNRAS, 370, 902
Khochfar S., Silk J., 2009, MNRAS, 397, 506
Kodama T. et al., 2004, MNRAS, 350, 1005
Krist J., Hook R., 2004, The TinyTim User's Guide. STScI, Baltimore, MD, p. 339
Kuntschner H., Lucey J. R., Smith R. J., Hudson M. J., Davies R. L., 2001, MNRAS, 323, 615
Larson R. B., 1974, MNRAS, 166, 585
Macchetto F., Pastoriza M., Caon N., Sparks W. B., Giavalisco M., Bender R., Capaccioli M., 1996, A&AS, 120, 463
McGaugh S. S., Schombert J. M., de Blok W. J. G., Zagursky M. J., 2010, ApJ, 708, L14
McIntosh D. H., Guo Y., Hertzberg J., Katz N., Mo H. J., van den Bosch F. C., Yang X., 2008, MNRAS, 388, 1537
Malin D. F., Carter D., 1983, ApJ, 274, 534
Mihos J. C., Hernquist L., 1996, ApJ, 464, 641
Morganti R. et al., 2006, MNRAS, 371, 157
Naab T., Johansson P. H., Ostriker J. P., 2009, ApJ, 699, L178
Prochaska J. X., Gawiser E., Wolfe A. M., Castro S., Djorgovski S. G., 2003, ApJ, 595, L9
Quinn P. J., 1984, ApJ, 279, 596
Saglia R. P., Colless M., Baggley G., Bertschinger E., Burstein D., Davies R. L., McMahan R. K., Wegner G., 1997, in Annaboldi M., Da Costa G. S., Saha P., eds, 2nd Stromlo Symp 116, The Nature of Elliptical Galaxies. Astron. Soc. Pac., San Francisco, p. 180
Sandage A., Visvanathan N., 1978, ApJ, 225, 742
Sarzi M. et al., 2008, in Knapen J., Mahoney T., Vazdekis A., eds, ASP Conf. Ser. Vol. 390, Pathways Through an Eclectic Universe. Astron. Soc. Pac., San Francisco, p. 218
Schawinski K. et al., 2007, ApJS, 173, 512
Schweizer F., Seitzer P., 1992, AJ, 104, 1039
Schweizer F., Seitzer P., Faber S. M., Burstein D., Dalle Ore C. M., Gonzalez J. J., 1990, ApJ, 364, L33
Searle L., Sargent W. L. W., Bagnuolo W. G., 1973, ApJ, 179, 427
Springel V., 2005, MNRAS, 364, 1105
Springel V., Di Matteo T., Hernquist L., 2005, MNRAS, 361, 776
Toomre A., 1977, in Tinsley B. M., Larson R. B., eds, Evolution of Galaxies and Stellar Populations. Yale University Observatory, New Haven, CT, p. 401
Trager S. C., Faber S. M., Worthey G., González J. J., 2000, AJ, 120, 165
van Dokkum P. G., 2005, AJ, 130, 2647
Worthey G., 1994, ApJS, 95, 107
Yi S. K. et al., 2005, ApJ, 619, L111
Young L. M., 2002, AJ, 124, 788

This paper has been typeset from a TEX/LATEX file prepared by the author.